Heliyon 11 (2025) e42105

Contents lists available at ScienceDirect

Heliyon

journal homepage: www.cell.com/heliyon

Research article

Microwave assisted palladium catalyzed carbon-carbon bond formation to synthesise novel benzimidazole derivatives and their Photophysical properties, molecular docking, and DFT study

Vijayabharathi Sundharaj , S. Sarveswari *

Department of Chemistry, School of Advance Sciences, Vellore Institute of Technology Vellore, Tamil Nadu, 632014, India

A B S T R A C T

In the present study, novel benzimidazole compounds are synthesized, utilizing Suzuki coupling and acid-amine coupling reaction. The formation of all synthesized derivatives was confirmed through various spectroscopic techniques, including ^{1}H, ^{13}C, Carbon DEPT-135, H-H COSY, HSQC, and HRMS. The UV–Vis and fluorescence spectra of all synthesized compounds were recorded. Particularly, among all synthesized compounds, compound **9o** (304.06 nm) exhibited the higher λ_{max} in UV–Vis spectroscopy, while compound **9j** (396.16 nm) exhibited the highest emmision intensity in fluorescence spectroscopy. Furthermore, density functional theory (DFT) calculations were performed at the B3LYP/6-31G′(d,p) foundational level set. These calculations aimed to predict the chemical reactivity of the newly synthesized benzimidazole derivatives by assessing parameters such as the HOMO-LUMO energy gap value, ionization potential, electrostaic potential, electron affinity, electronegativity, global hardness, and softness energy values. Subsequently, a molecular docking analysis was performed on all synthesized derivatives on a protein associated with Bcl-2 in conjunction with venetoclax, with compound **9g** (−10.77 kcal/mol) indicating the most significant binding affinity among the compounds investigated.

1. Introduction

Benzimidazole, constitutes a heterocyclic aromatic compound wherein a benzene ring is fused at 4 and 5 positions of an imidazole ring, [1]. Benzimidazole derivatives play a vital role in various therapeutic areas, acting as key components in antifungal, anti-inflammatory, and antitumor agents. Their unique chemical framework facilitates interactions with biological targets, making them invaluable in drug design [2]. This versatility ensures their continued relevance in advancing modern medicine and scientific innovation it has a great deal of promise for usage in pharmacological and biological applications [3,4] based on their importance, several drugs have been developed such as samatasvir, ridinalazole, temlisartan and flubendazole are shown in Fig. 1 [5,6] and they were found in the treatment of several diseases including epilepsy, diabetes and infertility [7]. Benzimidazole scaffold shows various biological activities such as antihelminitic[8], antitumor [9,10], anthelmintic [11], antimicrobial [12], anticancer [13], antiviral [14], antibacterial [15] and antiparasitic [16] activities, and because of their interactions with various proteins, RNA, and DNA, they are essential to the activity of many biologically significant molecules [17]. Due to the broad range of pharmacological characteristics of this chemical scaffold in the field of drug discovery, benzimidazole and its analogs have been the focus of extensive investigation to clarify their inventive uses in treating intricate diseases like cancer. The benzimidazole derivatives were found to exhibit outstanding anticancer capabilities against various cancer cell lines [18]. As a benzimidazole derivative, telmisartan is known to cause early apoptosis in cancerous cells [19]. An important target in the assessment of anticancer drugs is the inhibition of Bcl-2 protein [20]. It has

* Corresponding author.
E-mail address: ssarveswari@vit.ac.in (S. Sarveswari).

https://doi.org/10.1016/j.heliyon.2025.e42105
Received 1 October 2024; Received in revised form 11 January 2025; Accepted 17 January 2025
Available online 22 January 2025

been determined that some benzimidazole and its substituted derivatives are new inhibitors of Bcl-2 and/or tyrosine kinase. These compounds reported to impact important signaling pathways, exhibiting significant anticancer activity [21,22]. Recent literature has demonstrated that benzimidazole derivatives potentially impede the biosynthesis of microbial nucleic acids and proteins [23], thereby inhibiting the growth of diverse microorganisms [24–27].

Benzimidazole fluorescent probes are highly valued in chemical and biological sensing due to their excellent photophysical properties, including strong UV–visible absorption, bright fluorescence, high quantum yield, and good photostability [28]. They are designed to selectively bind to metal ions like Zn^{2+}, Cu^{2+}, Fe^{2+}, and Hg^{2+}, as well as to respond to pH changes and interact with biomolecules such as proteins and nucleic acids, making them useful in environmental monitoring, medical diagnostics, and biochemical research [29]. The probes are synthesized by functionalizing the benzimidazole core to enhance their selectivity and sensitivity.

Recent studies highlight their applications in detecting metal ions and monitoring pH changes in various samples [30]. Annulated benzimidazoles, recognized for their extensive π-conjugation and planar configurations, assume a important function in the realm of advanced optoelectronics, encompassing organic light-emitting diodes (OLEDs) and laser technologies [31,32]. In the context of benzimidazole, the conjugated nitrogen atoms present in the imidazole moiety demonstrate a very good affinity heightened affinity for proton donor and acceptor sites within the same molecular framework, analogous to water [33]. Consequently, the photophysical characteristics of the benzimidazole unit have been effectively modulated through the process of protonation. The electroluminescent devices, such as fluorescent and phosphorescent light-emitting diodes, are fabricated from bipolar hybrids including triphenylamine-oxadiazole, triphenylamine-benzimidazole, carbazole-oxadiazole, carbazole-benzimidazole, and triphenylamine-carbazole-benzothiadiazole [34–36]. The incorporation of nitrogen within the imidazole structure serves as an effective sensor for metal ions, thus prompting the advancement of selective detection methodologies for metal ions and anions, an area of increasing significance due to its critical role across a variety of environmental, clinical, and chemical domains [37]. Therefore, the investigation of photophysical properties pertaining to polycyclic benzimidazole has emerged as a prominent research focus in recent times.

In the present investigation, we successfully synthesized the novel compound tert-butyl 2-(5-(4-(2-(4-bromophenyl)acetamido) phenyl)-1*H*-benzo[*d*]imidazole-2-yl)pyrrolidin-1-carboxylates. A thorough characterization of all newly synthesized entities was performed utilizing NMR and High-Resolution Mass Spectrometry (HRMS) to ensure the structure [38,39]. Ultraviolet–Visible (UV–Vis) and Fluorescence (FL) spectra were obtained in acetonitrile solvent at room temperature with a concentration of 2×10^{-5} M. Moreover, molecular docking was employed as a valuable methodology to investigate the interaction of the synthesized biologically active compounds with target proteins, with particular emphasis on ligands containing analogous heterocyclic moieties present in our compound, which are known to act as inhibitors in the interaction of Bcl-2 protein with venetoclax. In addition, density functional theory (DFT) calculations were applied to accurately forecast various molecular properties, including optimized geometric structures, the HOMO-LUMO energy gap, ionization potential, electron potential, electron affinity, electronegativity, as well as global hardness and softness energy values, thereby providing a comprehensive understanding of the molecular characteristics.

2. Result and discussion

2.1. Chemistry

The synthetic pathway employed for the synthesis of tert-butyl 2-(5-bromo-1*H*-benzo[*d*]imidazole-2-yl)pyrrolidine-1-carboxylate derivatives (**9a-9p**) are shown in scheme-1 and all synthesized derivatives shown in Fig. 2. In the initial stage of synthesis, the benzimidazole scaffolds are cyclized using 4-bromobenzene-1,2-diamine (**1**) and (tert-butoxycarbonyl)proline (**2**). The coupling reagent HATU is utilized along with the DIPEA base to facilitate the formation of *tert*-butyl 2-(5-bromo-1H-benzo[d]imidazole-2-yl) pyrrolidine-1-carboxylate (**3**) [40], which is subsequently subjected to a Suzuki coupling reaction with compound-**3** and 4-amino phenyl boronic acid (**4**) in the presence of a Pd catalyst, resulting in the formation of tert-butyl 2-(5-(4-aminophenyl)-1*H*-benzo[d] imidazole-2-yl)pyrrolidine-1-carboxylate (**5**) [41]. The next step involves an acid amine coupling reaction compound-**5** with

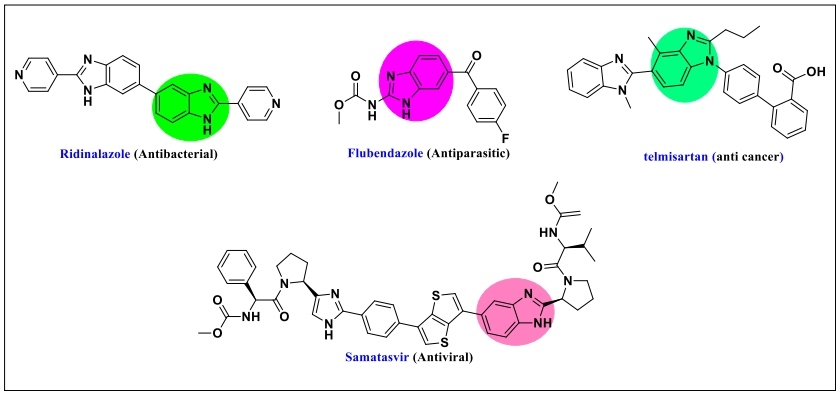

Fig. 1. Biologically active benzimidazole drugs.

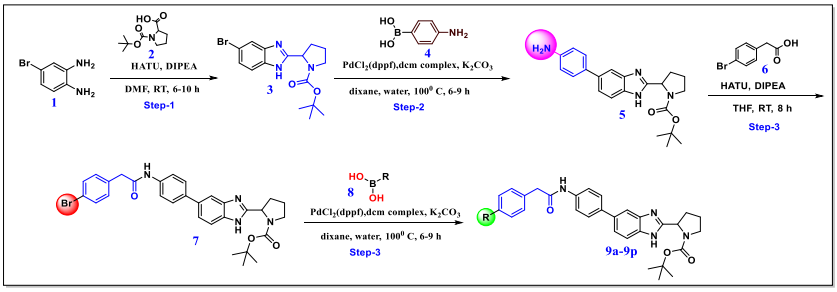

Scheme 1. Synthesis of benzimidazole derivatives **9a-9p**.

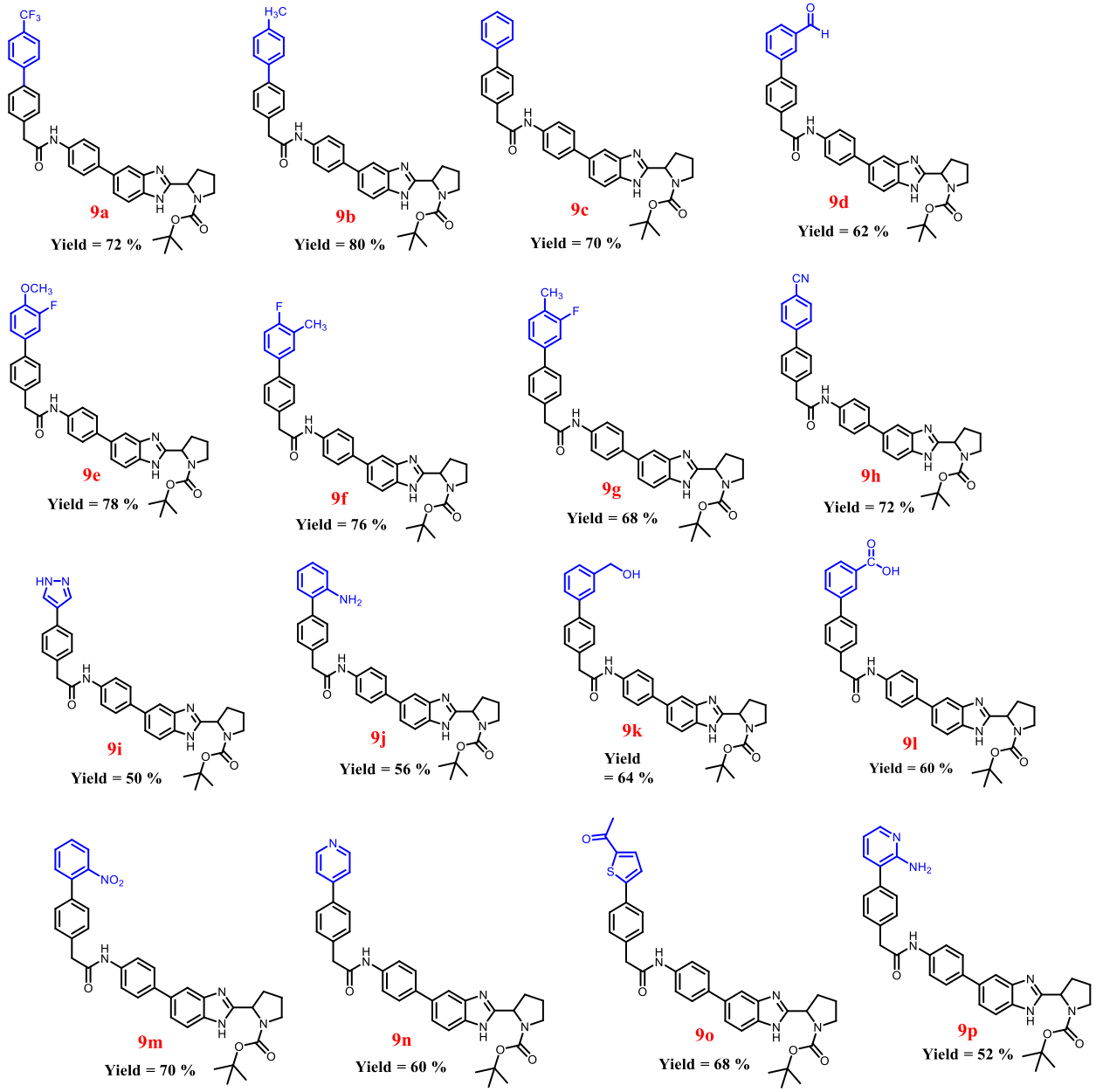

Fig. 2. Synthesized derivatives **9a-9p**.

2-(4-bromophenyl)acetic acid, HATU, and DIPEA base, yielding tert-butyl 2-(5-(4-(2 (4-bromophenyl)acetamido)phenyl)-1*H*-benzo [*d*]imidazole-2-yl)pyrrolidine-1-carboxylate (**7**). Finally, the desired compound was synthesized via a Suzuki coupling reaction that incorporated a variety of substituted boronic acids, palladium catalyst, and K_2CO_3 serving as the base, resulting in a product yield ranging from 50 % to 80 % Fig. 3. The aryl (R) series includes substituents such as methyl, CF_3, OCH_3, aldehyde, as well as halogens like chloro- and fluoro-, in addition to heterocyclic moieties such as 1*H*-pyrazole, pyridine, 1-(thiophen-2-yl)ethan-1-one, and pyridin-2-amine shown in Table 3. The corresponding spectra of these synthesized compounds, which are characterized by ^{1}H NMR, ^{13}C NMR, and HRMS, can be found in the supporting information. Furthermore, the reaction scheme, as illustrated in Scheme 2, was optimized, with additional particulars detailed in Table 1.

Several solvents, bases, and Pd catalysts were used in optimization processes with a model molecule **9b**. A high 80 % yield was obtained using a dioxane-water solvent combination with palladium catalyst and K_2CO_3 as the base. A 62 % yield was achieved using CS_2CO_3 as the base and Toluene-water as the solvent with Pd catalyst, as well as several bases including K_3PO_4, K_2CO_3, NaOH, and DIPEA. Additionally, with K_2CO_3 as the base, the THF-water combination with the previous bases produced a satisfactory yield of 56 %. Different Pd catalysts, $PdCl_2(OAc)_2$ and $PdCl_2(dppf)_2$, were used in subsequent studies.

3. Photophysical properties

3.1. UV–Vis and Fluorescence spectroscopy

The normalized electronic absorption and fluorescence spectra pertaining to the benzimidazole-based organic molecules, which were analyzed at a concentration level of 2×10^{-5} M dissolved in acetonitrile, as illustrated in Figs. 4 and 5, provide profound and significant insights into the complex photophysical properties inherent to these molecular structures. In a comprehensive manner, as delineated in Table 2, the various photophysical parameters reveal that the specific substitution patterns, particularly those involving amide, imidazole NH, and ester functional groups, induce remarkable and notable shifts in the absorption and emission spectra of the compounds under investigation. The UV–Vis spectroscopy analysis also shows that the exact substituents present in the benzimidazole derivatives and specifics the molecular structure have a significant impact on the different electronic transitions, such as not being limited to π-π^* and n-π^* transitions. These observable effects are additionally underscored by the prominent bathochromic shifts that are recorded in the absorption spectra, particularly for those compounds that incorporated with electron-withdrawing groups such as nitro, which effectively lower the energy gap that exists between the ground and excited electronic states, thereby facilitating absorption at significantly longer wavelengths. Conversely, it has been observed that the presence of electron-donating groups tends to induce hypsochromic shifts, which result in the absorption occurrs at shorter wavelengths. The fluorescence spectra that were recorded under an excitation wavelength of 290 nm exhibited emission across a range of 347–397 nm, characterized by varying intensities, thereby illustrating the significant impact that different substituents exert on the electronic environment and, as a direct consequence, on both non-radiative and radiative decay rates associated with the excited states.

The high fluorescence intensities observed in compounds with -CF_3, OCH_3, and -F substituents. Furthermore, the Stokes shifts was calculated using equation-1 that were quantified, which ranged from 0.1162×10^4 to 0.8039×10^4, emphasize the remarkable sensitivity of the fluorescence method in detecting emitted photons against a backdrop of low interference, despite the conventional association of large Stokes shifts with reduced fluorescence quantum yields, thereby presenting an intriguing paradox. The quantum

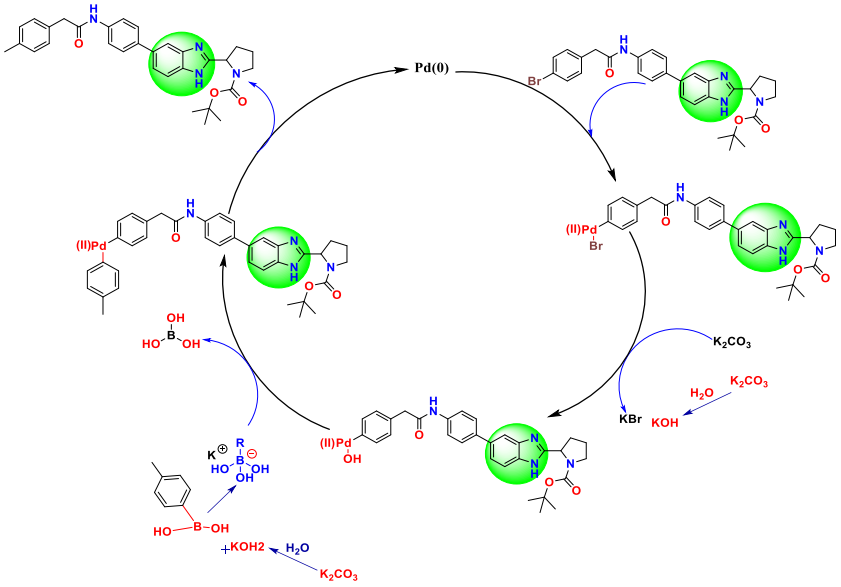

Fig. 3. Plausible mechanistic pathway for the reaction involving compound **9b**.

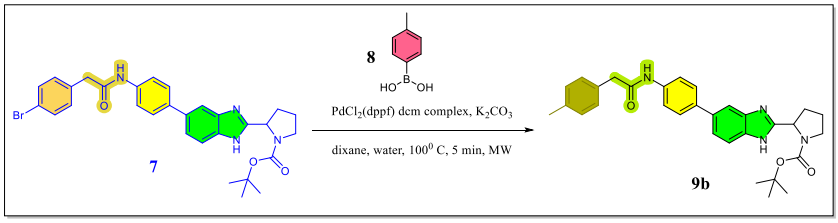

Scheme 2. Optimization reaction of compound **9b**.

Table 1
Optimization of the reaction involving compound **9b** utilizing various bases, solvents, and (Pd cat. = palladium catalysts).

S. No	Compound Code	Catalyst	Solvent	Base	Yield
1	**9b**	Pd cat.	Toluene/H_2O	CS_2CO_3	62
2	**9b**	Pd cat.	Toluene/H_2O	K_2CO_3	60
3	**9b**	Pd cat.	Toluene/H_2O	K_3PO_4	55
4	**9b**	Pd cat.	Toluene/H_2O	NaOH	44
5	**9b**	Pd cat.	Toluene/H_2O	DIPEA	Trace
6	**9b**	Pd cat.	1,4 dioxane/H_2O	CS_2CO_3	64
7	**9b**	Pd cat.	**1,4 dioxane**/H_2O	K_2CO_3	**80**
8	**9b**	Pd cat.	1,4 dioxane/H_2O	K_3PO_4	66
9	**9b**	Pd cat.	1,4 dioxane/H_2O	NaOH	64
10	**9b**	Pd cat.	1,4 dioxane/H_2O	DIPEA	Trace
11	**9b**	Pd cat.	THF/H_2O	CS_2CO_3	40
12	**9b**	Pd cat.	THF/H_2O	K_2CO_3	56
13	**9b**	Pd cat.	THF/H_2O	K_3PO_4	48
14	**9b**	Pd cat.	THF/H_2O	NaOH	44
15	**9b**	Pd cat.	THF/H_2O	DIPEA	Trace
16	**9b**	$PdCl_2$(OAc)2	1,4 dioxane/H_2O	K_2CO_3	70
17	**9b**	$PdCl_2$(dppf)2	1,4 dioxane/H_2O	K_2CO_3	62

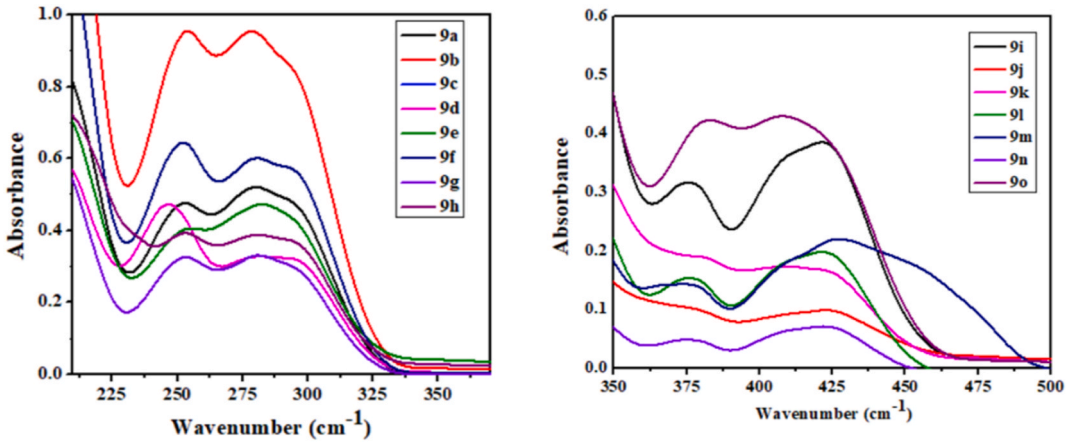

Fig. 4. Unnormalized electronic absorption spectra of synthesized derivatives (**9a**-**9p**) at room temperature, concentration (2×10^{-5} M) in acetonitrile solvent.

yield was calculated by using eq. (2), The highest quantum yield, which was quantitatively determined to be 0.4582 for compound **9a**, serves as a clear indicator of its superior efficiency in fluorescence, whereas compound **9d**, in contrast, exhibited the lowest quantum yield, which can likely be attributed to the destabilizing influence exerted by its electron-withdrawing substituents on the electronic excited state that is responsible for fluorescence emission. Additionally, the molar extinction coefficients that were calculated by the Beer–Lambert law demonstrated commendable absorptive capacities across the spectrum of compounds analyzed, with values ranging from 0.7211×10^4 M^{-1} cm^{-1} to 6.0800×10^4 M^{-1} cm^{-1}, thereby further corroborating the robust photophysical response exhibited by these benzimidazole derivatives in their interaction with light.

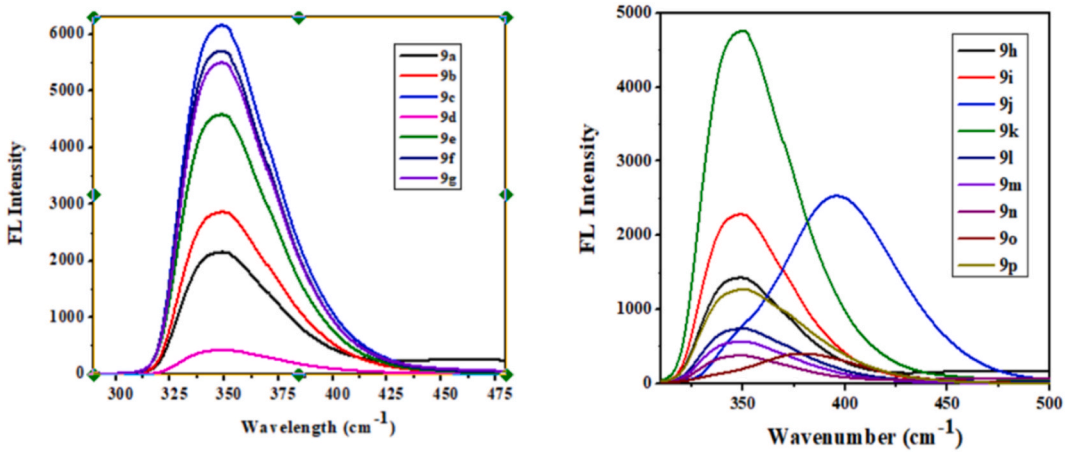

Fig. 5. Unnormalized emission spectra of synthesized derivatives (**9a-9p**) at room temperature, concentration (2×10^{-5} M) in acetonitrile solvent.

Table 2
Photophysical spectroscopic data of synthesized compounds **9a-9p** in acetonitrile solution (2 × 10-5 M) at 25 °C.

Entry	Compound code	λ_{max} absorbance	λ_{max} emission	Stokes shift $\Delta \times 10^4$	Molar extinction coefficient $\times 10^4$ (ε)	Quantum yield (ϕ_f)
1	**9a**	280.64	348.70	0.6954	5.1789	0.4982
2	**9b**	279.53	350.25	0.7222	9.5711	0.0275
3	**9c**	283.59	348.65	0.6580	3.9905	0.0686
4	**9d**	292.45	347.33	0.5402	2.3415	0.0586
5	**9e**	283.53	349.15	0.6628	4.7487	0.0858
6	**9f**	281.71	348.92	0.6837	6.0800	0.0833
7	**9g**	282.42	349.43	0.6789	3.3187	0.1493
8	**9h**	292.91	350.47	0.5607	3.7489	0.0464
9	**9i**	296.51	349.43	0.5107	3.8186	0.0541
10	**9j**	300.46	396.16	0.8039	0.9546	0.0582
11	**9k**	293.97	350.75	0.1296	2.3845	0.0188
12	**9l**	296.86	348.92	0.5025	1.6225	0.0488
13	**9m**	296.15	349.70	0.5170	1.9871	0.0305
14	**9n**	293.85	349.97	0.5457	3.9050	0.0110
15	**9o**	304.06	379.16	0.6513	2.1879	0.0239
16	**9p**	298.28	351.41	0.5068	0.7211	0.1903

4. Density Functional theory (DFT) studies

The Density Functional Theory (DFT) methodology has been shown to possess a distinct advantage in the computational analysis of organic and inorganic compounds due to its enhanced efficacy relative to alternative methodologies. The geometrical optimization

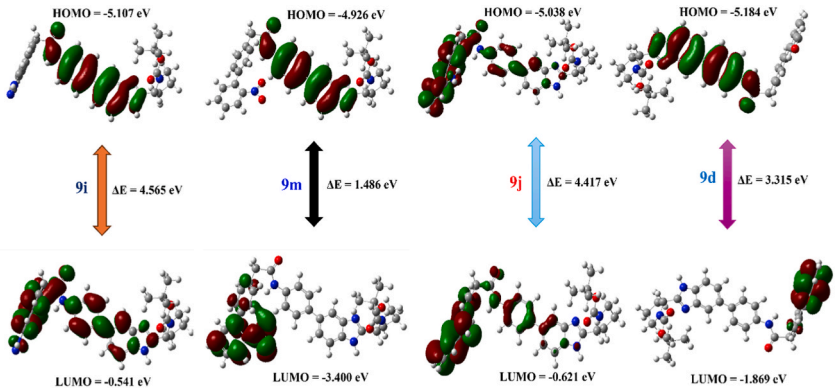

Fig. 6. Highest occupied molecular orbital (HOMO) and lowest unoccupied molecular orbital (LUMO) diagrams of current molecules **9i**, **9m**, **9j** and **9d** calculated at the B3LYP/6-31G' (d, p) basis set level.

calculations of the synthesized compound were conducted utilizing the Gaussian 09 software [42] and the GaussView 5.0 [43] molecular visualization toolkit, employing the B3LYP/6-31G'(d,p) [44] basis set within the density functional theory (DFT) framework. The electronic characteristics of the most energetically favorable configuration were investigated, encompassing the highest occupied molecular orbital (HOMO), the lowest unoccupied molecular orbital (LUMO), and various global reactivity descriptors. A molecular electrostatic potential (MEP) map of the optimized compounds was generated, byutilizing the B3LYP functional within the DFT framework, which was facilitated by the GaussView 5.0 software suite.

4.1. Frontier Molecular Orbital (FMO) analysis

The electronic characteristics and molecular reactivity of compounds are significantly influenced by frontier molecular orbitals (FMO), specifically the highest occupied molecular orbital (HOMO) and the lowest unoccupied molecular orbital (LUMO), which serve as representations of electron donors and acceptors, respectively [45]. It is observed that molecules possessing higher HOMO energy levels exhibit a greater capacity for electron donation, whereas those with lower LUMO energy levels demonstrate a stronger inclination towards accepting electrons. The evaluation of FMO energy plays a pivotal role in the assessment of molecular stability and reactivity among chemical compounds. The energy diffence existing between the HOMO and LUMO, commonly known as the energy gap (ΔE gap), is of fundamental importance as it directly impacts the stability, intramolecular electron cloud transfer, chemical behavior, molecular softness, and hardness of the compounds under investigation. Through the FMO analysis synthesised compounds depicted in in Fig. 6 and data in Table-3, the information regarding the energy levels of HOMO, LUMO, as well as the diffence between the two, along with other essential reactivity parameters, is revealed. In the case of compounds **9a**-**9p**, it is observed that the electron density of the HOMO is prominently concentrated in the benzimidazole moiety and the amide functional group, whereas the electron density of the LUMO is primarily situated over the substituted amide group. The FMO diagrams presented in Fig. 6 highlight the electron density transition from the HOMO to the LUMO in selected compounds, with a particular focus on those exhibiting the highest and lowest energy differences. Especially, compounds **9d**, **9h**, **9i**, and **9j** showcase an enhanced electron density in the LUMO, which can be attributed to the presence of electron-withdrawing substituents such as formyl, NO_2, carboxylic acids, and cyano groups. Conversely, electron-donating substituents like NH_2 and OH do not significantly impact the electron density of the HOMO originating from the parent moiety and amide group. HOMO and LUMO value comparisons through the investigation of LUMO values (−3.440eV, −1.892eV) in compounds **9m** and **9h** highlights their strong electron accepting characteristic, the HOMO (−5.252eV, −5.218eV) between compounds **9a** and **9h** shows a substantial electron donation capability. While the analysis of these compounds, especially **9i** and **9j**, shows the largest energy gaps, in contrast to compounds **9m** and **9d**, which show much smaller energy gaps, a bigger energy gap indicates lower reactivity, increased stability, and insulating qualities.

A diminished HOMO−LUMO gap denotes an elevated level of reactivity, consequently enhancing the likelihood of interactions with biological molecular targets. Fig. 6 delineates the frontier molecular orbitals (FMOs) of compounds that demonstrated significant binding affinity during the docking investigations [46,47]. A diminished ΔE gap signifies a tendency toward electron excitation, augmented chemical reactivity, and increased molecular softness, while an elevated energy (ΔE) gap correlates with decreased reactivity and enhanced chemical hardness. This observation suggests a substantial charge separation within the molecule, which may influence its interactions in various chemical environments. The derived reactivity descriptors provide critical insights into the electronic structure, behavior, and prospective chemical interactions of the synthesized compounds (**9a**−**9p**) [48]. The ability of the

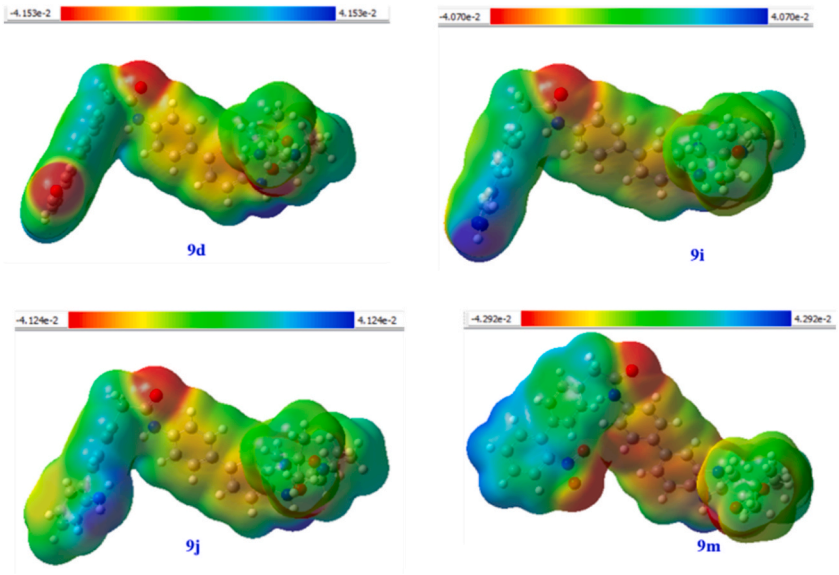

Fig. 7. Molecular electrostatic potential of compounds **9i**, **9j**, **9m** and **9d** calculated at the B3LYP/6-31G (d, p) basis set level.

compounds to either gain or lose electrons is shown by the computed ionization potential and electron affinity. However, their chemical hardness and electronegativity highlight their overall stability and electron-attracting capabilities. As a reactivity descriptor, electrophilicity measures the possibility that a molecule may undergo electrophilic reactions. These descriptors are essential in elucidating the reactivity trends of these compounds across a range of chemical processes [49]. The insights obtained from these computations will further enhance the categorization and identification of the compounds based on their unique reactivity characteristics.

4.2. Molecular Electrostatic Potential (MEP)

In the present study, the initial stage used the molecular electrostatic potential (MEP) map to carefully examine the electron distribution at the reactive molecular sites to make predictions about the molecule's interaction modes and create associations with physicochemical descriptors [51]. The MEP technique creates a critical balance by combining the repulsive forces of the nuclei (shown by a positive charge, which indicates nucleophilic reactivity in blue) and the attractive forces of the electrons (shown by a negative charge, which indicates electrophilic potential in yellow and red) [52]. The green color observed in MEP visualizations signifies an intermediate potential value. The wide range of colors seen in the MEPs clearly shows the differences in electrostatic potential levels, which are ordered in descending order from red to yellow to blue to green, as shown in Fig. 7. Whereas the red zones, which are mostly found next to the carbonyl groups, indicate places of high electron density, the green-shaded areas, which are especially concentrated around the phenyl rings in all compounds, indicate areas of intermediate potential. These color changes are crucial for identifying the molecular locations most likely to engage in intermolecular interactions as well as for highlighting the locations most susceptible to electrophilic and nucleophilic attacks [53]. The increase in the blue areas suggests that the compounds are more electrophilic, that in turn increases the substrate's capacity to identify the binding site by means of the electrostatic interactions formed between the substrate and the receptor. In MEP diagrams, the blue-colored positive regions signify nucleophilic attack due to diminished electron density, whereas the red, orange, or yellow negative areas correspond to electrophilic attack, associated with elevated electron density. Green is used to signify the neutral areas. High electron density is seen in all molecular entities, especially around the nitrogen atoms in the benzimidazole structure, the carbonyl amide group, and close to electron-deficient substituents like the formyl group in compound **9d**, the fluorine substituent in compound **9e**, the cyano group in compound **9h**, and the keto group in compound **9o**, as shown by the red-colored negative regions in Fig. 7. On the different conjunction, the low electron density regions shown in blue are found around the N-H group in the benzimidazole structure, the N-H group that is connected to the amide functional group, and around substituent groups like the amino group in compound **9j**, the pyrazole group in compound **9i**, and the hydroxyl groups in compounds **9k** and **9l**.

5. Molecular docking

The Molecular docking study were executed utilizing the standard parameters of AutoDock4 [54], which included the specification of 30 genetic algorithm iterations. The receptor-ligand complex underwent a thorough analysis to ascertain the binding free energy, with the most favorable docking conformations being prioritized based on the minimal binding energy [55]. Subsequent to the docking procedures, an analysis was performed employing Discovery Studio Visualizer 2017 [56] to evaluate the hydrogen bonding interactions, hydrophobic contacts, and various other non-covalent interactions between the ligand and the receptor's active site. The molecular interactions were rendered visually to clarify the binding affinity and specificity of the ligand in relation to the target protein, thereby offering valuable insights into the molecular foundations of the observed biological activity [57]. This study delves

Table 3
HOMO−LUMO Energies (eV) and the Computed Global Reactivity Parameters of the Most Stable Configurations of Compounds **9a**−**9p** at the B3LYP/6-31G'(d,p) basis set Level. ΔE denotes the energy gap (ELUMO − EHOMO). IP represents the ionization potential (=−EHOMO). EA signifies the electron affinity (=−ELUMO). χ is defined as the electronegativity (=(IP + EA)/2). η refers to the chemical hardness (=(IP − EA)/2). S is characterized as the chemical softness (=1/2η). μ denotes the chemical potential (=−(IP + EA)/2). ω represents the electrophilic index (=μ2/2η) [50].

S. No	Code	EHOMO	ELUMO	ΔE (eV)	IP (eV)	EA (eV)	X (eV)	μ (eV)	H (eV)	S (eV)	ω (eV)
1	**9a**	−5.218	−1.516	3.701	5.218	1.516	3.367	−3.367	1.851	0.54	3.062
2	**9b**	−5.112	−0.914	4.197	5.112	0.914	3.013	−3.013	2.099	0.476	2.162
3	**9c**	−5.127	−0.998	4.129	5.127	0.998	3.062	−3.062	2.064	0.484	2.271
4	**9d**	−5.184	−1.869	3.315	5.184	1.869	3.526	−3.526	1.657	0.603	3.751
5	**9e**	−5.145	−1.032	4.113	5.145	1.032	3.088	−3.088	2.056	0.486	2.319
6	**9f**	−5.15	−1.032	4.117	5.15	1.032	3.091	−3.091	2.059	0.485	2.32
7	**9g**	−5.149	−1.092	4.056	5.149	1.092	3.12	−3.12	2.028	0.493	2.41
8	**9h**	−5.252	−1.892	3.359	5.252	1.892	3.572	−3.572	1.681	0.594	3.795
9	**9i**	−5.107	−0.541	4.565	5.107	0.541	2.824	−2.824	2.283	0.438	1.746
10	**9j**	−5.038	−0.621	4.417	5.038	0.621	2.829	−2.829	2.208	0.452	1.812
11	**9k**	−5.098	−0.973	4.125	5.098	0.973	3.035	−3.035	2.062	0.484	2.233
12	**9l**	−5.149	−1.514	3.635	5.149	1.514	3.331	−3.331	1.817	0.55	3.053
13	**9m**	−4.926	−3.44	1.486	4.926	3.440	4.183	−4.183	0.743	1.345	11.77
14	**9n**	−5.219	−1.475	3.743	5.219	1.475	3.347	−3.347	1.872	0.534	2.992
15	**9o**	−5.205	−1.821	3.383	5.205	1.821	3.513	−3.513	1.692	0.591	3.646
16	**9p**	−5.185	−0.889	4.296	5.185	0.889	3.037	−3.037	2.148	0.465	2.146

into the molecular interactions and binding affinities of a set of synthesized derivatives, **9a**−**9p**, in relation to the Bcl-2 protein, analyzed alongside venetoclax, a known cancer therapeutic. The research employed a detailed in silico docking approach to reveal the intricate binding dynamics of these compounds, aiming to comprehend their potential in cancer treatment. The results of this computational investigation are presented comprehensively in Table 4, Fig. 8 displays stacked bar charts that depict protein interactions with binding affinity which serves as a crucial reference for understanding the binding behaviors of these derivatives with the Bcl-2 protein (PDB:6O0k). In this study, the synthesized derivatives acted as ligands, while the Bcl-2 protein served as the receptor in the molecular docking experiments. The molecular docking yielded significant data on the binding energies and interactions between the derivatives and the protein. The binding affinities, recorded between −8.20 and −10.77 kcal/mol, highlight the structural diversity and flexibility of the synthesized compounds, providing insight into their potential as cancer therapeutics. The range of interactions identified in this research demonstrates the different binding mechanisms that the synthesized derivatives employ in interacting with the target protein. This suggests that these compounds could be promising candidates for further investigation in the field of cancer therapy. This findings offer a strong foundation for future research, laying the groundwork for exploring these analogs as potential therapeutic agents. Their structural versatility and favorable binding affinities present them as valuable subjects for continued study in the development of cancer treatments. Notably, compound **9g** (illustrated in Fig. 11 with both two-dimensional and three-dimensional interactions) exhibited remarkable potential due to its extraordinarily elevated binding affinity of −10.77 kcal/mol towards the complex formed by Bcl-2 and venetoclax, indicating its suitability as a leading candidate for further investigation. Comprehensive examination of the ligand-protein complex illuminated the complex dynamics that dictate this interaction. [58] The study revealed the existence of significant conventional hydrogen bonds between compound **9g** and several crucial amino acid residues within the protein framework. Among these, the residues GLY A:145 and ASN A:143 were particularly critical, as they played a vital role in fortifying the ligand's integration within the protein architecture. The hydrogen bonds established by compound **9g**, particularly with the residues GLY A:145 and ASN A:143, are paramount for the stabilization of the ligand within the receptor, as illustrated in Fig. 11. These interactions emphasize the specificity and selectivity of the binding event, thereby accentuating the structural integrity of the complex. Such interactions play a pivotal role in influencing the overall strength and stability of the molecular assembly, thereby highlighting the therapeutic potential of compound **9g**, especially in oncological applications. In addition to compound **9g**, compound **9h** (depicted in Fig. 9 with both two-dimensional and three-dimensional interaction representations) also demonstrated a significant binding affinity of −10.75 kcal/mol. The interaction of this compound, characterized by pi-sigma and van der Waals forces with critical amino acid residues, introduces additional complexity to its binding mechanism, thereby reinforcing its promise as a viable therapeutic agent. Similarly, compound **9f** (as represented in Fig. 10) exhibited a robust binding affinity of −10.45 kcal/mol. The interaction of compound **9f** with residues such as GLY A:145 through conventional hydrogen bonding significantly augmented the stability of the ligand-protein complex, positioning it as a potential candidate for further exploration in cancer therapeutics. The cumulative findings from these interactions underscore the structural and functional significance of these compounds in the formulation of future therapeutic strategies.

6. Experimental section

6.1. Materials and methods

All the chemicals and solvents were purchased commercially BLD and Merck Brand. The synthesis of tert-butyl 2-(5-(4-(2-(4-bromophenyl)acetamido)phenyl)-1*H*-benzo[*d*]imidazole-2-yl)pyrrolidine-1-carboxylate followed previously described methods. Proton (^{1}H) and Carbon (^{13}C) NMR spectra were recorded on a Bruker Avance 400 spectrometer, with chemical shifts (δ) referenced to the residual solvent signals $CDCl_3$: (7.26) for ^{1}H and (77.16) for ^{13}C NMR; dimethyl sulfoxide-d_6 (2.50) for ^{1}H and (39.50) for ^{13}C. Shifts are given in ppm and coupling constants (J) in Hz. Abbreviations used include s-singlet, d-doublet, dd-doublet of doublet, t-triplet, m-multiplet, and br-broad. HR ESI-MS values were measured on a Xeo G2-XS QTof (Waters) and are reported in *m/z*. A JASCO V-670 spectrometer was used to produce absorption spectra. Using a Hitachi F-7000 FL spectrofluorophotometer, steady-state fluorescence spectra were obtained through excitation at the peak of absorption. Silica gel (100–200 mesh) was employed in for column chromatography, while Macherey-Nagel 60 F245 aluminum-backed silica gel plates were utilized for analytical thin-layer chromatography (TLC). The Stoke's Shift and the quantum yield were determined through the reported mathematical expression 1 and 2 [59].

$$\Delta\nabla = 10^{7} \;/\; \lambda_{\max(\text{Absorption})} - 10^{7} \;/\; \lambda_{\max(\text{Emission})} \qquad 1$$

$$\phi f = \phi_{R}.\, A_{R}/A.I/I_{R}.n^{2}R/n^{2} \qquad 2$$

6.2. General procedure for the synthesisis of compounds (9a-9p)

The tert-butyl2-(5-(4-(2-(4-bromophenyl)acetamido)phenyl)-1H-benzo[d]imidazole-2-yl)pyrrolidin-1-carboxylate derivative **7** (1 equivalent) K_2CO_3 (3.0 equivalent) and substituted boronic acid **8a** (2.5 equivalent) was taken in 10 mL of 1,4-dioxane and water mixture. After degassing the reaction mixture using nitrogen gas. About 0.05 equivalent of the catalyst ($PdCl_2$(dppf)dcm) was added to the reaction mixture and was subjected to the heating at 100 °C for about 20 min. The progress of the reaction was monitored by TLC, after the completion of the reaction 50 mL of cold water was added to quench the reaction. Then the product was extracted using ethyl acetate the organic layer resulting from this was concentrated and dried to get the solid product. The crude product is purified using

Table 4
Molecular docking results of synthesized compounds (**9a**–**9p**) Bcl-2 with venetoclax protein (PDB: 6O0k).

S. No	Compound code	Binding energy (kcal/mol)	Interacting residues (amino acids)
1	**9a**	−9.41	TYR A:202, VAL A:133, MET A:115, TYR A:108, GLNA:118, ARG A:107, PHEA:104, ARG A:146, LEU A:137, VALA:148, ALA A:100, LEUA:137, VAL A:148, ALA A:100, LEU A:119, GLY A:145
2	**9b**	−10.39	HIS A:184, ARG A:127
3	**9c**	−10.35	PHE A:112, LEU A:137, ALA A:149, ARG A:146, PHE A:104, ASN A:143, GLY A:145
4	**9d**	−9.80	TRP A:144, GLY A:145, TYR A:202, TYR A:108, PHE A:104, ARG A:146, ALA A:149, LEU A:137, ASP A:111
5	**9e**	−10.10	LEU A:137, VAL A:133, ALA A:149, ARG A:146, TRP A:144, PHE A:104, TYRA:108, TYR A:202, GLY A:145, ASN A:192
6	**9f**	−10.46	ASN A:192, GLY A:145, TRP A:188, TRPA:144, ARG A:146, PHE A:112, VAL A:156, PHE A:104, ALA A:149, VAL A:133, LEU A:137
7	**9g**	−10.77	TRP A:144, TYR A:108, PHE A:104, GLY A:145, ASN A:143, ALA A:149, LEU A:137, VAL A:133, MET A:155
8	**9h**	−10.75	ALA A:100, ARG A:146, ALA A:149, LEU A:137, VAL A:133
9	**9i**	−9.17	TYR A:202, ASN A:143, GLY A:145, ALA A:149, VAL A:133, LEU A:137, TYR A:108, PHE A:104, MET A:115
10	**9j**	−9.81	ALA A:100, ARG A:107, ASP A:103, TYR A:202, GLY A:145, TYR A:108, PHE A:104, ALA A:149, LEU A:137, MET A:115
11	**9k**	−9.78	TYRA:202, ALAA:100, GLYA:145, ARGA:146, TYRA:108, PHEA:104, META:115, ALA A:149, VALA:133, LEUA:137
12	**9l**	−9.22	ARG A:106, GLN A:99, ALA A:100, TYR A:202, LEU A:137, ARG A:146, ALA A:149
13	**9m**	−8.67	LEU A:137, VAL A:133, ALA A:149, TYR A:108, PHE A:104, TRP A:144, GLY A:145
14	**9n**	−9.11	TRP A:144, TYR A:202, GLY A:145, ARG A:146, TYR A:108, PHE A:104, ALA A:149, LEU A:137, VAL A:133
15	**9o**	−9.49	MET A:115, GLN A:118, LEU A:119, HIS A:120
16	**9p**	−8.20	ASP A:191, TRP A:188, VAL A:142, PHE A:138, TYR A:180, ARG A:139

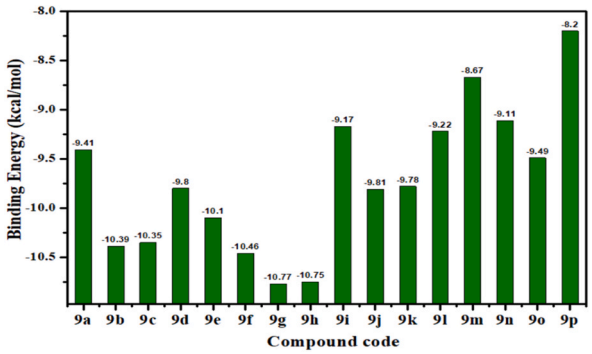

Fig. 8. Stacked bar charts illustrating protein interactions with 6o0k-complex throughout the showcasing binding energy of protein–ligand contacts.

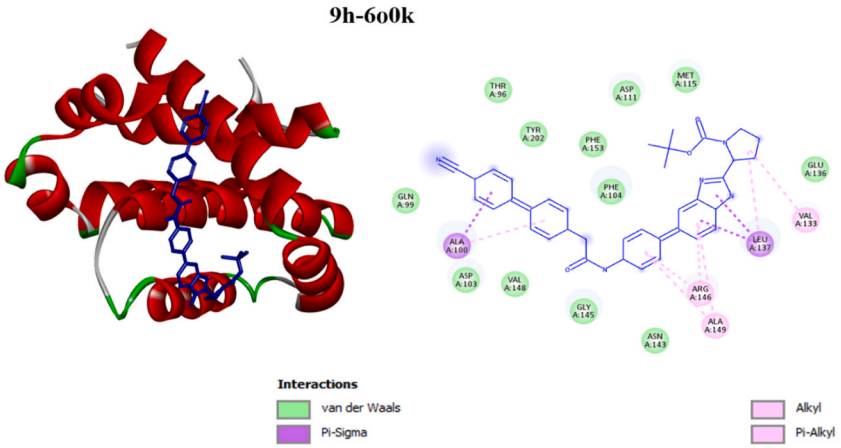

Fig. 9. 2D and 3D binding interactions of compound **9h** with Protein (6O0K).

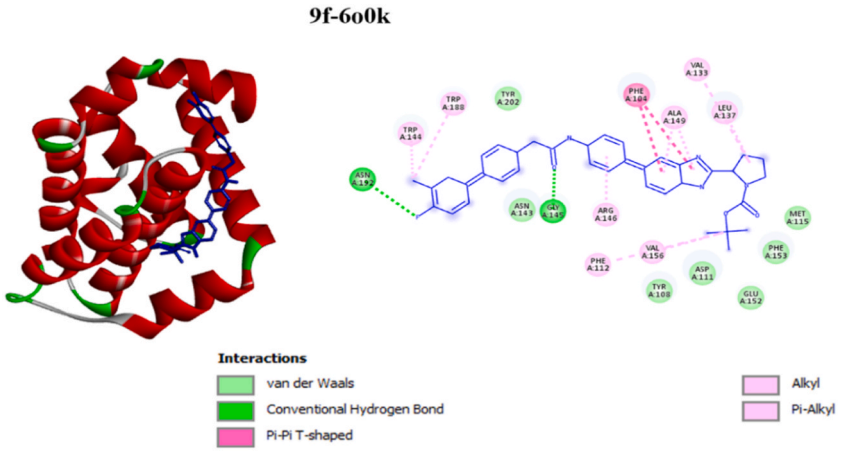

Fig. 10. 2D and 3D binding interactions of compound **9f** with Protein (6O0K).

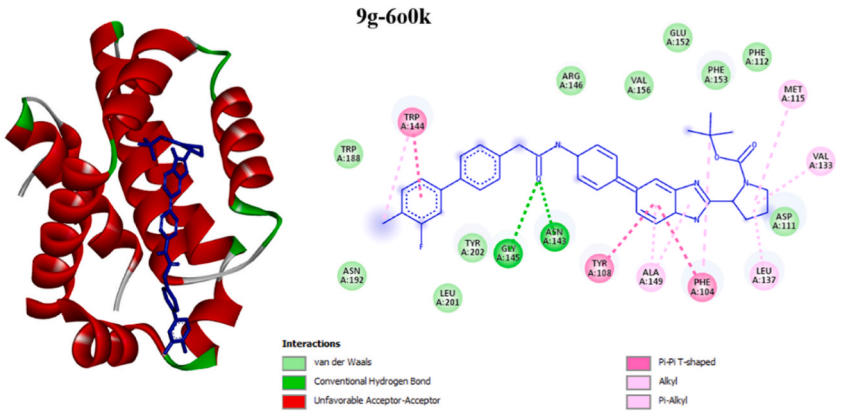

Fig. 11. 2D and 3D binding interactions of compound **9g** with Protein (6O0K).

column chromatography to isolate the product **9a**. The procedure is repeated with the other derivatives using different substituted boronic acids **8b-8p** to get **9b** to **9p.** The synthetic procedure and spectral data of the compounds **9a** to **9p** are given in supplementary information.

7. Conclusion

In current work a new benzimidazole derivatives were sucessfuly synthesized via Suzuki coupling and acid amine coupling with excellent yield. Subsequently, the obtained compounds were characterized by ^{1}H, ^{13}C, DEPT-135 NMR and HRMS spectrum. DFT calculations were used to predict stability and reactivity properties. DFT calculations focused for the prediction of chemical reactivity of the newly synthesized benzimidazole derivatives by evaluating parameters such as the HOMO-LUMO energy gap value, ionization potential, electron affinity, electronegativity, global hardness, and softness energy values. On the other hand, FMOs analysis shows the molecule energy gap for **9a** and **9h** (−5.252, −5.218Kcal/mol) indicates less reactive capability whereas the compound **9m** and **9h** (−3.440, −1.892 Kcal/mol) indicates the more reactivity. The most responsive sites for nucleophilic and electrophilic attack were predicted by the MEP analysis. Additionally, molecular docking studies showed that the synthesized compounds have a high ability to interact with **6O0K** protein. These findings suggest that the synthesized compounds could be a suitable candidate for the development of new anticancer lead molecule. Further planning to expand the benzimidazole moiety and conduct biological studies on cancer cell lines.

CRediT authorship contribution statement

Vijayabharathi Sundharaj: Writing – original draft, Conceptualization. **S. Sarveswari:** Writing – review & editing, Validation, Conceptualization.

Supportiing information

The synthetic procedure, identification data and ^{1}H, ^{13}C, Carbon DEPT-135 NMR the compounds' HRMS spectra can be found in this article's supporting information.

Declaration of competing interest

The authors declare the following financial interests/personal relationships which may be considered as potential competing interests:S Sarveswari reports financial support, administrative support, article publishing charges, and equipment were provided by Vellore Institute of Technology. S Sarveswari reports a relationship with Vellore Institute of Technology that includes: employment. If there are other authors, they declare that they have no known competing financial interests or personal relationships that could have appeared to influence the work reported in this paper.

Acknowledgment

The authors would like to express their gratitude to the Vellore Institute of Technology in Vellore for providing the infrastructure, characterization facilities, and fellowship that allowed them to complete this work. The authors are grateful to Dr. V. Vijayakumar for his support and advice.

References

[1] G. Kumari, S. Dhillon, P. Rani, M. Chahal, D.K. Aneja, M. Kinger, Development in the synthesis of bioactive thiazole-based heterocyclic hybrids utilizing phenacyl bromide, ACS Omega 9 (17) (2024 Apr 16) 18709–18746.
[2] S. Venugopal, B. Kaur, A. Verma, P. Wadhwa, M. Magan, S. Hudda, V. Kakoty, Recent advances of benzimidazole as anticancer agents, Chem. Biol. Drug Des. 102 (2) (2023 Aug) 357–376.
[3] M. Tuncbilek, T. Kiper, N. Altanlar, Synthesis and in vitro antimicrobial activity of some novel substituted benzimidazole derivatives having potent activity against MRSA, Eur. J. Med. Chem. 44 (3) (2009) 1024–1033.
[4] M.L. Richards, S.C. Lio, A. Sinha, H. Banie, R.J. Thomas, M. Major, M. Tanji, J.C. Sircar, Substituted 2-phenyl-benzimidazole derivatives: novel compounds that suppress key markers of allergy, Eur. J. Med. Chem. 41 (8) (2006) 950–969.
[5] J.P. Bilello, L.B. Lallos, J.F. McCarville, M. La Colla, I. Serra, C. Chapron, J.M. Gillum, C. Pierra, D.N. Standring, M. Seifer, In vitro activity and resistance profile of samatasvir, a novel NS5A replication inhibitor of hepatitis C virus, Antimicrob. Agents Chemother. 58 (8) (2014) 4431–4442.
[6] S. Khanna, Clostridial vaccines in the pipeline, Drugs Future 45 (9) (2020).
[7] A. Giovine, M. Muraglia, M.A. Florio, A. Rosato, F. Corbo, C. Franchini, B. Musio, L. Degennaro, R. Luisi, Synthesis of functionalized arylaziridines as potential antimicrobial agents, Molecules 19 (8) (2014) 11505–11519.
[8] P.N. Preston, Synthesis, reactions, and spectroscopic properties of benzimidazoles, Chem. Rev. 74 (3) (1974) 279–314.
[9] V. Rajendiran, M. Murali, E. Suresh, S. Sinha, K. Somasundaram, M. Palaniandavar M, Mixed ligand ruthenium (II) complexes of bis (pyrid-2-yl)-/bis (benzimidazol-2-yl)-dithioether and diimines: study of non-covalent DNA binding and cytotoxicity, Dalton Trans. 1 (2008) 148–163.
[10] J. Mann, A. Baron, Y. Opoku-Boahen, E. Johansson, G. Parkinson, L.R. Kelland, S. Neidle, A new class of symmetric bisbenzimidazole-based DNA minor groove-binding agents showing antitumor activity, J. Med. Chem. 44 (2) (2001) 138–144.
[11] R. Kenchappa, Y.D. Bodke, A. Chandrashekar, S. Telkar, K.S. Manjunatha, M.A. Sindhe, Synthesis of some 2, 6-bis (1-coumarin-2-yl)-4-(4-substituted phenyl) pyridine derivatives as potent biological agents, Arab. J. Chem. 10 (2017) S1336–S1344.
[12] A.H. El-masry, H.H. Fahmy, S.H. Ali Abdelwahed, Synthesis and antimicrobial activity of some new benzimidazole derivatives, Molecules 5 (12) (2000) 1429–1438.
[13] N. Shrivastava, M.J. Naim, M.J. Alam, F. Nawaz, S. Ahmed, O. Alam, Benzimidazole scaffold as anticancer agent: synthetic approaches and structure–activity relationship, Arch. Pharm. 350 (6) (2017) e201700040.
[14] M. Tonelli, M. Simone, B. Tasso, F. Novelli, V. Boido, F. Sparatore, Antiviral activity of benzimidazole derivatives. II. Antiviral activity of 2-phenylbenzimidazole derivatives, Bioorg. Med. Chem. 18 (8) (2010) 2937–2953.
[15] D. Song, S. Ma, Recent development of benzimidazole-containing antibacterial agents, ChemMedChem 11 (7) (2016) 646–659.
[16] J. Valdez, R. Cedillo, A. Hernandez-Campos, L. Yepez, F. Hernandez-Luis, G. Navarrete-Vazquez, A. Tapia, R. Cortes, M. Hernández, R. Castillo, Synthesis and antiparasitic activity of 1H-benzimidazole derivatives, Bioorg. Med. Chem. Lett. 12 (6) (2002) 2221–2224.
[17] N. Perin, K. Bobanović, I. Zlatar, D. Jelić, V. Kelava, S. Koštrun, V.G. Marković, K. Brajša, M. Hranjec, Antiproliferative activity of amino substituted benzo [b] thieno [2, 3-b] pyrido [1, 2-a] benzimidazoles explored by 2D and 3D cell culture system, Eur. J. Med. Chem. 125 (2017) 722–735.
[18] S. Venugopal, B. Kaur, A. Verma, P. Wadhwa, M. Magan, S. Hudda, V. Kakoty, Recent advances of benzimidazole as anticancer agents, Chem. Biol. Drug Des. 102 (2) (2023) 357–376.
[19] M. Matsuyama, K. Funao, K. Kuratsukuri, T. Tanaka, Y. Kawahito, H. Sano, J. Chargui, J.L. Touraine, N. Yoshimura, R. Yoshimura, Telmisartan inhibits human urological cancer cell growth through early apoptosis, Exp. Ther. Med. 1 (2) (2010) 301–306.
[20] M. Bruncko, T.K. Oost, B.A. Belli, H. Ding, M.K. Joseph, A. Kunzer, D. Martineau, W.J. McClellan, M. Mitten, S.C. Ng, P.M. Nimmer, Studies leading to potent, dual inhibitors of Bcl-2 and Bcl-xL, J. Med. Chem. 50 (4) (2007) 641–662.
[21] B. Chu, F. Liu, L. Li, C. Ding, K. Chen, Q. Sun, Z. Shen, Y. Tan, C. Tan, Y. Jiang, A benzimidazole derivative exhibiting antitumor activity blocks EGFR and HER2 activity and upregulates DR5 in breast cancer cells, Cell Death Dis. 6 (3) (2015) e1686 e1686.
[22] V.L. Nayak, N. Nagesh, A. Ravikumar, C. Bagul, M.V. Vishnuvardhan, V. Srinivasulu, A. Kamal A, 2-aryl benzimidazole conjugate induced apoptosis in human breast cancer MCF-7 cells through caspase independent pathway, Apoptosis 22 (2017) 118–134.
[23] S. Gatfaoui, N. Issaoui, A. Mezni, F. Bardak, T. Roisnel, A. Atac, H. Marouani, Synthesis, structural and spectroscopic features, and investigation of bioactive nature of a novel organic-inorganic hybrid material 1H-1, 2, 4-triazole-4-ium trioxonitrate, J. Mol. Struct. 1150 (2017) 242–257.
[24] M. Kemal Yılmaz, S. Ince, S. Yılmaz, M. Keles, Palladium (II) catalyzed Suzuki CC coupling reactions with imino-and amino-phosphine ligands, Inorg. Chim. Acta. 482 (2018) 252e258.
[25] C. Xi, Y. Wu, X. Yan, Cis-Fashioned palladium (II) complexes of 2-phenylbenzimidazole ligands: synthesis, characterization, and catalytic behavior towards Suzuki–Miyaura reaction, J. Organomet. Chem. 693 (2008) 3842e3846.
[26] M.J. Kim, M.J. Jung, Y.J. Kim, H.K. Sung, J.Y. Lee, S.J. Ham, C.P. Park, Sublimable bis (β-iminoenolate) palladium (II) complexes and their application as catalysts in Suzuki-Miyaura reactions, Tetrahedron Lett. 59 (2018) 2989e2993.
[27] B. Mahjour, Y. Shen, W. Liu, T. Cernak, A map of the amine–carboxylic acid coupling system, Nature 580 (7801) (2020) 71–75.
[28] E. Horak, P. Kassal, I. Murković Steinberg, Benzimidazole as a structural unit in fluorescent chemical sensors: the hidden properties of a multifunctional heterocyclic scaffold, Supramol. Chem. 30 (10) (2018) 838–857.

[29] S. Anbu, A. Paul, K. Surendranath, N.S. Solaiman, A.J. Pombeiro, A benzimidazole-based new fluorogenic differential/sequential chemosensor for Cu^{2+}, Zn^{2+}, CN^{-}, $P_2O_7^{4-}$, DNA, its live-cell imaging and pyrosequencing applications, Actuators B Chem 337 (2021) 129785.

[30] a) S. Pise, N. Dey, Modulation in charge transfer characteristics of flexible bis-benzimidazole probes: independent sensing mechanisms for Hg^{2+} and F^{-}, Dalton Trans. (2024);
b) S.H. Chen, K. Jiang, Y. Xiao, X.Y. Cao, M. Arulkumar, Z.Y. Wang, Recent endeavors on design, synthesis, fluorescence mechanisms and applications of benzazole-based molecular probes toward miscellaneous species, Dyes Pigments 175 (2020) 108157.

[31] R. Langer, Drug deliver. Drugs on target, Science 293 (5527) (2001) 58–59.

[32] V.B. Kovalska, D.V. Kryvorotenko, A.O. Balanda, M.Y. Losytskyy, V.P. Tokar, S.M. Yarmoluk, Fluorescent homodimer styrylcyanines: synthesis and spectral-luminescent studies in nucleic acids and protein complexes, Dyes Pigments 67 (1) (2005) 47–54.

[33] J. Schönamsgruber, A. Hirsch, Benz-bisimidazole-bridged perylenes–linearly expanded chromophores, Eur. J. Org. Chem. 10 (2015) 2167–2174.

[34] F. Dumur, F. Goubard, Triphenylamines and 1, 3, 4-oxadiazoles: a versatile combination for controlling the charge balance in organic electronics, N. J. Chem. 38 (6) (2014) 2204–2224.

[35] R.N. Francke, R.D. Little, Optimizing electron transfer mediators based on arylimidazoles by ring fusion: synthesis, electrochemistry, and computational analysis of 2-aryl-1-methylphenanthro [9, 10-d] imidazoles, J. Am. Chem. Soc. 136 (1) (2014) 427–435.

[36] S. Gong, Y. Zhao, C. Yang, C. Zhong, J. Qin, D. Ma, Tuning the photophysical properties and energy levels by linking spacer and topology between the benzimidazole and carbazole units: bipolar host for highly efficient phosphorescent OLEDs, J. Phys. Chem. 114 (11) (2010) 5193–5198.

[37] K.L. Haas, K.J. Franz, Application of metal coordination chemistry to explore and manipulate cell biology, Chem. Rev. 109 (10) (2009) 4921–4960.

[38] S. Qiu, L. Liu, X. Jin, A.Q. Zhang, K. Wu L.S. Wang, Vibrational spectroscopic investigation and DFT studies on 2, 2′, 4, 4′-tetrabromodiphenyl ether, Spectrochim. Acta A 77 (2010) 572e578.

[39] R.J. Qu, X.S. Zhang, Q. Zhang, X. Yang, Z.Y. Wang, L.S. Wang, Experimental and theoretical study on IR and NMR spectra of several tetrachlorinated diphenyl sulfides, Spectrochim. Acta A 811 (2011) 261e269.

[40] V. Bhatt, S.D. Samant, S. Pednekar, Efficient one-pot HATU mediated coupling of dicarboxylic acid and amines for the synthesis of diamide at ambient temperature, Lett. Org. Chem. 14 (10) (2017) 764–768.

[41] K.S. Sali, Y. Baqi, Microwave-assisted palladium-catalyzed cross-coupling reactions: generation of carbon–carbon bond, Catalysts 10 (1) (2019) 4.

[42] M.J. Frisch, G.W. Trucks, H.B. Schlegel, G.E. Scuseria, M.A. Robb, J.R. Cheeseman, G. Scalmani, V. Barone, B. Mennucci, G.A. Petersson, H. Nakatsuji, Gaussian 09, Revision D. 01, Gaussian, Inc., Wallingford CT, 2009, p. 620. See also: URL, http://www.gaussian.com.

[43] R.D. Dennington, T.A. Keith, J.M. Millam, GaussView 5.0, Gaussian. Inc., Wallingford, 2008, p. 20.

[44] D. Becke, Density-functional thermochemistry. III. The role of exact exchange, J. Chem. Phys. 98 (1993) 5648–5652, https://doi.org/10.1063/1.464913.

[45] a) N.D. Chavan, V. Vijayakumar, Synthesis, DFT studies on a series of tunable quinoline derivatives, RSC Adv. 14 (29) (2024) 21089–21101;
b) N.D. Chavan, V. Vijayakumar, Palladium catalyzed carbon-carbon bond formation on tunable quinolines with DFT study, J. Mol. Struct. (2024) 139739.

[46] S. Rathod, D. Bhande, S. Pawar, K. Gumphalwad, P. Choudhari, H. More, Identification of potential hits against fungal lysine deacetylase Rpd3 via molecular docking, molecular dynamics simulation, DFT, in-silico ADMET and drug-likeness assessment, Chem. Afr. 7 (2) (2024) 1151–1164.

[47] B. Kosar, C. Albayrak, Spectroscopic investigations and quantum chemical computational study of (E)-4-methoxy-2-[(p-tolylimino) methyl] phenol, Spectrochim. Acta 78 (1) (2011) 160–167.

[48] K. Burke, Perspective on density functional theory, J. Chem. Phys. 136 (15) (2012).

[49] A.S. Badran, A. Ahmed, A.I. Nabeel, M.A. Ibrahim, Ring opening ring closure reactions with 5, 9-diethyl-7-(chromon-3-yl)-7-hydroquinolino [3′, 4′: 5, 6] pyrano [3, 2-c] quinoline-6, 8 (5H, 9H)-dione with some 1, 2-binucleophiles: synthesis, characterization, DFT study and biological activity, J. Mol. Struct. 1298 (2024 Feb 15) 137030.

[50] a) N.A. Alshaye, M.A. Ibrahim, A.S. Badran, Nucleophilic transformation of 3-substituted-6, 8-dimethylchromones with phenylhydrazine under various reaction conditions: theoretical, spectroscopic characterization and in silico ADME studies, J. Mol. Struct. 1297 (2024 Feb 5) 137006;
b) A.R. Kumar, L. Ilavarasan, G.S. Mol, S. Selvaraj, M. Azam, P. Jayaprakash, M. Kesavan, M. Alam, J. Dhanalakshmi, S.I. Al-Resayes, A. Ravi, Spectroscopic (FT-IR, FT-Raman, UV–Vis and NMR) and computational (DFT, MESP, NBO, NCI, LOL, ELF, RDG and QTAIM) profiling of 5-chloro-2-hydroxy-3-methoxy-benzaldehyde: a promising antitumor agent, J. Mol. Struct. 1298 (2024 Feb 15) 136974.

[51] M.A. Ibrahim, A.S. Badran, M.M. Attai, N.M. El-Gohary, Z. Hussain, O. Farouk, Synthesis, Structural Characterization, Fukui functions, DFT Calculations, Molecular docking and biological efficiency of some novel heterocyclic systems, J. Mol. Struct. 30 (2024 May) 138815.

[52] A.S. Badran, M.A. Ibrahim, Recyclization of 3-substituted-6, 8-dimethylchromones with some heterocyclic enamines: spectroscopic, quantum calculations (HOMO–LUMO, MEP, NLO), biological evaluation, and ADME investigation, J. Heterocycl. Chem. 61 (8) (2024 Aug) 1224–1247.

[53] M.A. Mostafa, M.A. Ibrahim, A.S. Badran, Spectroscopic elucidation, quantum chemical computations (FMO, HOMO–LUMO, MEP, NLO), and biological activity on some novel heterocyclic compounds using 3-substituted-6, 8-dimethylchromones, Synth. Commun. 54 (18) (2024 Sep 16) 1523–1550.

[54] G.M. Morris, R. Huey, W. Lindstrom, M.F. Sanner, R.K. Belew, D.S. Goodsell, A.J. Olson, AutoDock4 and AutoDockTools4: automated docking with selective receptor flexibility, J. Comput. Chem. 30 (16) (2009 Dec) 2785–2791.

[55] S.C. Ja'afaru, A. Uzairu, I. Bayil, M.S. Sallau, G.I. Ndukwe, M.T. Ibrahim, A.T. Moin, A.M. Mollah, N. Absar, Unveiling potent inhibitors for schistosomiasis through ligand-based drug design, molecular docking, molecular dynamics simulations and pharmacokinetics predictions, PLoS One 19 (6) (2024 Jun 26) e0302390.

[56] D.S. Biovia, Discovery Studio Visualizer, 936, 2017, pp. 240–249. San Diego, CA, USA.

[57] A. Mermer, H.A. Bayrak, S. Alyar, M. Alagumuthu, Synthesis, DFT calculations, biological investigation, molecular docking studies of β-lactam derivatives, J. Mol. Struct. 1208 (2020) 127891.

[58] P. Subhapriya, K. Sadasivam, M.M. Mohan, P.S. Vijayanand, Experimental and theoretical investigation of p–n alkoxy benzoic acid based liquid crystals–A DFT approach, Spectrochim. Acta, Part A 123 (2014) 511–523.

[59] K. George, P. Elavarasan, S. Ponnusamy, K. Sathananthan, Facile one-pot synthesis of functionalized quinoline-fused fluorescent dihydro/spiro-quinazolinone derivatives, ACS Omega 7 (24) (2022) 20605–20618.